V.D. Vijayanand, M. Mokhtarishirazabad, J. Peng, Y. Wang, M. Gorley, D.M. Knowles, M. Mostafavi

A novel methodology for estimating tensile properties in a small punch test employing in-situ DIC based deflection mapping

A novel methodology for estimating tensile properties in a small punch test employing in-situ DIC based deflection mapping

V.D. Vijayanand, M. Mokhtarishirazabad, J. Peng, Y. Wang, M. Gorley, D.M. Knowles, M. Mostafavi

A novel methodology for estimating tensile properties in a small punch test employing in-situ DIC based deflection mapping

V.D. Vijayanand[1*], M. Mokhtarishirazabad[1], J. Peng[1,2], Y. Wang[3], M. Gorley[3], D.M. Knowles[1], M. Mostafavi[1]

[1]Department of Mechanical Engineering, University of Bristol, Bristol BS8 1TR, UK
[2]School of Mechanical Engineering, Changzhou University, Changzhou 213164 China
[3]United Kingdom Atomic Energy Authority, Culham Science Centre, Abingdon OX14 3DB, UK
*Correspondence: vd.vijayanand@bristol.ac.uk; Tel: +44 7448169725

Abstract

Determining tensile properties from small punch test is being pursued actively in the nuclear industry due to the limited volume of material such tests use compared with standard tests which can be critical when considering active or development samples. One of the crucial challenges in harnessing the full potential of this technique is formulating methodologies which correlate the small punch specimen's deflection to equivalent uniaxial tensile properties. Existing approaches for correlation rely on deflection obtained from a single point on the small punch test specimen, used with empirical equations to make the correlation. However, the deflection and strain accumulation in a small punch specimen is highly heterogeneous and data from a single point does not represent the gross deformation evolving in the specimen. This data when used in conjunction with the empirical formulations for deriving equivalent uniaxial tensile properties, would not result in accurate identification of material properties. In this work we offer an alternative approach which uses the full field deflection of the specimen mapped through in-situ digital image correlation. The use of digital image correlation combined with inverse finite element analysis augments the existing method of material properties identification from single point deflection data thereby significantly improving the reliability of the measurements.

1. Introduction

Over the last few decades there has been a considerable impetus for developing small scale specimen testing techniques for evaluating mechanical properties of materials. It is the multiple advantages these techniques offer that has propelled its sustained advancement and is being actively pursued as a reliable method in situations where estimation of mechanical properties using conventional testing techniques is not viable. The paramount application of the small specimen techniques is in the nuclear industry where determining mechanical properties of irradiated material using small specimen volume is crucial [1–5]. Small specimen testing has also found application in remnant life assessment of in-service components [6–10]. However, a key challenge lies in converting the properties determined by the small specimen testing techniques to those obtained from conventional standardised techniques.

1

Among several miniature specimen techniques, the small punch test is one of the most versatile as it has been used to deduce tensile [2,11,24–27], creep [8,9,28–30], fracture [2,31–33], ductile to brittle transition temperature [11,34–36] and fatigue properties [37]. In a small punch test, a thin specimen is clamped between two nondeformable dies and a rigid spherical punch is forced into the specimen. Elevated temperature tests carried out at constant load in force-controlled mode are used to obtain the time-displacement characteristics. Creep properties can hence be estimated from the time-displacement characteristics. Load-displacement curves can be obtained if the tests are carried out in a displacement-controlled mode when the penetration rate of the punch is held constant. The load-displacement characteristics can be used to obtain equivalent tensile and fracture properties. The wide acceptance of the small punch test has led to the development of a pre-normative code of practice by CEN [38]. This code lists the guidelines for designing a small punch test rig and gives details about the testing procedure. The code also describes various approaches for deriving creep, tensile and fracture properties.

The CEN code of practice outlines two approaches for obtaining equivalent tensile properties from displacement-controlled small punch tests. The first approach which had been widely pursued by several researches uses empirical correlations to convert parameters characterising the load-displacement curve to equivalent 0.2% proof strength and ultimate tensile strength [3,4,10–16] . Substantial research has also been pursued employing the second approach which envisages the use of Finite Element Modelling (FEM) as a tool to back-calculate the elastic and plastic properties to match the profile of the experimentally obtained load-displacement curve [17–23].

The inherent limitation in both these approaches stems from the fact that the load-displacement/deflection characteristics of the material which is pivotal in both these approaches is acquired from a single point on the specimen. In case of the load-deflection curve it is obtained from the central point of the deforming specimen using a linear variable differential transformer (LVDT). The load-displacement curve on the other hand is obtained by recording the displacement of the punch. However, the specimen's deflection contour resembles a hemispherical shell owing to the geometry of the punch. Mapping the entire deflection contour of the specimen would offer new perspectives to existing approaches for estimating equivalent uniaxial properties.

In this work a new methodology has been developed for estimating the elastic and plastic properties of 316L stainless steel utilising Digital Image Correlation (DIC) based in-situ deflection mapping and inverse finite element modelling (iFEM). Using DIC a wide deflection field could be mapped on the specimen. The mechanical properties were then back-calculated using FEM by matching the load-deflection characteristics obtained from multiple locations in the specimen.

2. Experiments and analysis

2.1 Material and characterisation

The chemical composition of 316L stainless steel is given in Table 1. Rods of 8 mm diameter were machined from 12 mm thick plates which were solution annealed at 1323±5 K for 30 minutes and water quenched. The initial grain size of the material which was determined by Heyn's intercept method was around 50±15 μm. Specimens of 1 mm were sliced from the heat-treated rods by electrical discharge machining. The final thickness of 0.5±0.005 mm of the small specimens was achieved by carefully grinding them manually with P800 and subsequently P1200 silicon carbide sandpapers. For DIC imaging a white primer was first applied on the specimen before spraying black speckle patterns on to its surface using an airbrush. Tensile specimen of gauge length 12 mm and diameter 6 mm was also machined from the solution treated rods. Uniaxial tensile testing was carried out on this specimen at a nominal strain rate of 1×10^{-3} s^{-1}. Optical micrographs were taken using Zeiss Axio Imager M2 optical microscope. Electron Back Scatter Diffraction (EBSD) images were taken using Zeiss Sigma HD VP field emission Scanning Electron Microscope. TSL OIM software was used for plotting Kernel Average Misorientation (KAM) Maps. An upper threshold of 1.5° was used to map the misorientation in these maps. The threshold used for grain boundary detection was 10°.

2.2 Small punch test rig

The small punch test rig was attached to a servo-hydraulic benchtop system. A punch displacement rate of 0.005 mms^{-1} was used in this study. The schematic of the small punch test rig used in this study is given in Fig.1. The dimensions of the specimen, dies, and punch (ceramic ball) were compliant with the CEN standard [38]. The principal dimensions of the test rig are given in Table 2. A first surface mirror inclined at an angle of 45° was placed in between the lower dies. The inclined mirror facilitated a less cumbersome access for acquiring DIC images from the speckled specimen surface. The test rig was aligned on the servo-hydraulic machine in such a way that the optical axis of the lens system, the plane normal of the mirror and the loading axis were all co-planar.

2.3 Stereo DIC system

The stereo DIC system comprised of Zeiss Discovery V12 microscope integrated with two LaVision Image M-lite 5M cameras. An illumination ring comprising of 42 LEDs was attached to the circumference of the lens. A 200×200 μm^2 micro-grid plate was used to calibrate the stereo DIC system. Details of the stereo DIC setup and calibration are furnished in Table 3. DaVis software Version

3

10.0.5 was used to process the acquired image and obtain the out of plane deflections. A subset size of 55 pixels and step size of 25 pixels were used for the analysis.

Stereo DIC systems maps have been widely used to estimate changes in shape and out of plane displacements [39–42]. These systems estimate the out of plane displacement (Z_D)in addition to in-plane displacements (X_D and Y_D) using a triangulation algorithm [43]. The triangulation algorithm establishes an analytic linear relationship between each of the camera's pixel coordinates and the actual coordinates. The actual coordinates of the point of interest are then estimated by solving the two linear systems corresponding to the two cameras by least square technique. The solution for the analytic relationship requires estimation of the cameras' extrinsic and intrinsic parameters which can be obtained by a calibration procedure. The extrinsic parameters are related to the positioning and orientation of the cameras. The intrinsic parameters are dependent upon the camera's optic centre and focal length. The calibration gives the scaling for in-plane displacements (X_D and Y_D), these parameters are essential for estimating Z_D. Though the calibration establishes the relationship between the actual and the camera coordinates, there are several uncertainties in Z_D values which are inherent due to the use of stereo system [43,44]. Further uncertainties are generated due to the use of an inclined mirror. These uncertainties, classified as systematic errors, can be quantified as opposed to random errors which arise due to quality of speckle patterning and image noise level [45].

2.4 Quantifying uncertainties attributed to stereo DIC system

Both the stereo angle [44] and the base line distance [43] influence the precision of displacements in the three actual coordinates. The precision of all the displacement values (X_D, Y_D and Z_D) deteriorates with decrease in stereo angle. In fact, the uncertainties in values of Z_D are much higher than those observed for X_D and Y_D. Changes in base line distance do not influence the accuracy of both X_D and Y_D significantly. However, the uncertainty in Z_D increases significantly with lower base line values.

As the mirror is inclined at an angle of 45°, the plane of the lens and the plane of the mirror are not parallel. This implies that while estimating the Z_D all the longitudinal points in the image are not in focus at the same instance. Further, the resolution in the out of plane direction is also dictated by the depth of field (DOF) of the imaging system. The DOF gives the estimate of how much the object can be moved perpendicular to the line of sight without appreciable change is focus. The DOF is related to the numerical aperture (NA) and the wavelength of light (λ) used for illumination through the following equation [46]

$$DOF = \frac{\lambda}{NA^2} \qquad [1]$$

For a wavelength of 550 nm (the average wavelength of light in the visible spectrum) the DOF of the system is around 0.6 mm. This implies that within the Z_D range of 0.6 mm, uncertainties attributed to the limitation in the lens system's DOF is minimum.

In order to quantify the uncertainties in Z_D arising due to the use of the mirror, stereo DIC measurements were carried out on a zero-strain field test on the calibrated setup. For this test a speckled surface was displaced towards the mirror (in the Z_D direction) at a rate of 0.005 mms^{-1} controlled by the machine's hydraulic power system. This machine displacement was then compared to Z_D estimated by the stereo DIC setup. As there were no variation in X_D and Y_D in the zero-strain field test, precise estimation of uncertainties in Z_D could be made using the zero-strain field test. The direction of Z_D in this test was congruent to the direction of the out of plane deflection of the deforming small punch specimen. This test was used to establish the 1) uncertainties of the Z_D in the central point and 2) the variation in the displacement values in the contour map. A circular region of interest (ROI) with a radius of approximately 1.6 mm was chosen for contour mapping using the DIC data during the zero-strain field test. It was ensured that subsequent DIC analysis on the actual small punch specimen was carried out on a circular area almost equal and concentric with respect to the one used in the zero-strain field test.

The variations between the machine estimated and the DIC estimated displacement values taken from the central point (CP) in the ROI for the range between 0-3 mm is shown in Fig. 2. The region of minimum deviation (±0.01 mm) between the two displacements is indicated in the figure. This region (which spanned around 0.65 mm) was between the machine estimated displacement of 0.6 to 1.25 mm. The extent of this region was approximately equal to the DOF calculated for this system. Despite the uncertainties arising due to the stereo set up and the usage of mirrors, the deviation of the DIC estimated out of plane displacement and the machine displacement was in the range of ±0.07 mm through the machine estimated displacement range from 0-2.7 mm and starts to deviate considerably for values greater that 2.7 mm. The small punch tests in this work were carried out in such a way that during the test the machine estimated displacement values lie within the range of 0.6-2.7 mm, which is indicated as the total displacement range in Fig. 2. This was done in order to obtain minimum deviation during the initial stages of the test. The displacement values during the initial stages of the test were crucial as they were used subsequently for estimating the elastic and plastic properties using iFEM.

The displacement contour map taken at a machine estimated displacement of 1.15 mm is shown in Fig. 3. The scatter in the displacement values estimated by DIC in the transverse (X direction) and longitudinal (Y direction) directions for this machine estimated displacement is compared in Fig. 4. The

scatter in the transverse direction was comparatively lower than what was observed in the longitudinal direction. The gradient in Z_D calculated in the transverse direction is due to the use of the inclined mirror. In the current analysis the Z_D along one half of the transverse direction was used for further analysis. This segment of interest (SOI) is indicated in both Figs. 3 and 4. The variation in Z_D along the SOI was in the range of ±0.005 mm in the displacement range from 0.6-2.7 mm. Further, the DOF is similar for all the points along the SOI as they all lie along the transverse direction.

3. Results and discussion

3.1. Load-deflection characteristics

The Load-deflection curve of 316 L stainless steel obtained from the central point of the DIC-analysed ROI is shown in Fig. 5. The DIC images estimated for central point deflections of 0 mm, 0.54 mm, 1.16 mm, 1.75 mm and the image after failure are given in Fig. 6. The DIC estimated 3D-contour maps at these deflections (except for the failed instance) are shown in Fig. 7. The DIC estimated deflection contours were concentric to the central point. The contour maps start to degenerate along the circumferential regions during the later stages of specimen deformation. This is because during the later stages, sharp curvature in the circumferential regions obstructs precise resolution of the speckle pattern by the DIC system. However, the deflections along the regions adjoining the central point could be mapped satisfactorily until the peak load. Beyond the central point deflection of 2.05, the DIC system could not resolve any data from the speckled specimen surface.

The five stages which correspond to various deformation modes [5,11,14,15,24,26] during the small punch are depicted in Fig.5 . Macrographs corresponding to these stages are given Fig. 8. These macrographs were taken on specimens interrupted after deflections which roughly correspond (± 0.01 mm) to the deflections depicted in Figs. 6 and 7. Stages I and II comprises elastic and plastic bending regimes respectively. During the first two stages the contact area between the punch and the specimen increases rapidly and there is no appreciable reduction in specimen thickness [2]. Stage III is the membrane stretching regime when the contact area does not increase significantly but the specimen thickness starts to reduce. Initiation of localised thinning was evident even at this stage (Fig. 8b). Further thinning and localised necking constitute the plastic instability regime (Stage IV). Thereafter, in Stage V due to material softening there is a drop in load and fracture propagates rapidly resulting in failure. It has been reported that in Stages I and II, the deformation is governed by elastic and plastic properties only. With the onset of Stage III, voids start to nucleate at regions which are highly strained. These voids coalescence during Stage IV which subsequently result in further localised thinning and failure [47]. The deformation behaviour of the specimen after the onset of Stage III can be completely simulated only by incorporating suitable damage models [11,18,26,47].

Though there is no apparent specimen thickness reduction in the plastic-elastic bending stage, strain gradients could still accumulate across the specimen. To probe the variations in strain evolution during Stage II in the specimen, EBSD based KAM maps (Fig.9) were obtained from the central point (Location A) and from a location at a radial distance of 0.6 mm from the central point (Location B) (Fig. 7). The KAM maps are used to get an estimate of the geometrically necessary dislocations and can be used to map localised strain gradients in the material [48–50]. It could be clearly seen that the misorientation in Location B was higher than in Location A. Though the deflection in Location A was higher than in Location B, the strain accumulation in the later region was higher than that observed from the central point.

During a constant displacement rate controlled uniaxial tension test, the strain accumulation within the gauge length of the specimen is relatively uniform up to the point of instability. This enables a straightforward conversion of the load-displacement data obtained in a uniaxial tensile test to engineering data. However, in a small punch test considerable strain gradient evolve in the specimen even during the initial stages of deformation. Therefore, load deflection characteristics obtained only from the central point or the singular punch displacement is not an ideal representative of the gross deformation behaviour occurring within the material during testing. Estimating several location specific deflections would enhance the understanding about the deformation characteristics of the material paving way for formulating better correlation with respect to uniaxial tensile properties.

3.2 Inverse finite element method (iFEM)

Deflection values up to the onset of stage III obtained from multiple locations on the specimen were used in an inverse finite element method (iFEM) which was formulated to determine the elastic and plastic properties of the material. The scheme of the iFEM used in this work is depicted in Fig. 10. There three main constituents of the of the iFEM framework which was used in the current analysis are -a) a geometrically representative finite element model b) a constitutive model for characterizing elastic and plastic flow behaviour of the material and c) an optimization procedure. These three aspects of the iFEM framework are described in the following sections.

3.2.1 Finite Element Model

The finite element model was generated using Abaqus CAE 6.14-1, the geometry of the model was identical to the dimensions used in the experiment. The punch, lower and upper dies were considered as rigid bodies. The deformable element type used for the modelling the specimen was a 4-node bilinear axisymmetric quadrilateral (CAX4R). A uniform element size of 0.03 mm was used for meshing the specimen geometry. The total number of elements in the specimen model was 2261. The

specimen was deformed until a punch displacement of 0.65 mm. This punch displacement would generate specimen deflection well within the Stage II deformation regime. The value of the friction coefficient used for modelling interaction between the punch and specimen was 0.2. A frictionless interaction was assumed between the die and specimen interface. Though values of the friction coefficient are material specific, its influence on the load deflection characteristics is negligible during the initial stages of specimen deformation [51].

3.2.2 Constitutive flow equation

The Young's Modulus (E) and the Poisson's ratio(v) were used to characterize the deformation behaviour in the elastic regime. The values of both these constants were optimised using iFEM. The Ludwigson constitutive equation was used to model the plastic flow behaviour as it gives an accurate description of flow behaviour of austenitic stainless steels [52–56]. The Ludwigson equation has an additional exponential term which considers the deviation from the Ramberg-Osgood model at lower strains [57].

The Ludwigson equation takes the following form

$$\sigma_p = K_1 \varepsilon_p^{n_1} + exp(K_2 + \varepsilon_p n_2) \qquad [2]$$

Where σ_p and ε_p are the true stress and true plastic strain respectively, $K_1, n_1, K_2 \ and \ n_2$ are empirical constants. The upper and lower bounds of the parameter values used in the analysis are given in Table 4.

3.2.3 Optimisation procedure

A genetic algorithm (GA) based procedure was implemented using MATLAB programming language for optimising the elastic and plastic properties. GA is an optimization tool which searches the global minima of objective functions [23,58]. Initially GA chooses a random population of parameter values within the given upper and lower bounds. It then obtains the values of the objective function based on various combination of the parameter values for each generation. The rank of each of these combinations is evaluated based on a fitness function which gauges the proximity to the minima. GA then refines the population in subsequent generations to obtain a better combination of parameters with improved fitness function-based ranking. The options set in the GA module are given in Table 5.

Two optimization techniques were formulated, a single-point optimisation (SPO) using the deflection obtained from the central point and another multi-point optimisation (MPO) using the deflections obtained from four points. Since the data extracted for the SPO technique was from the central point it is equivalent to acquiring specimen deflection from an LVDT. It can be therefore be argued that the

8

SPO technique is equivalent of performing iFEM using LVDT data. The four points were chosen for the MPO technique lie along the SOI indicated in Figs. 3 and 4. Apart from the one central point the other three points were placed at 0.6, 0.9 and 1.2 mm from the central point in the specimen's pre-deformed condition (Fig. 11). The rationale behind choosing these points was that they had distinct load-deflection characteristics, which would make the MPO technique more effective. The load displacement curve from the point placed at a distance of 0.3 mm from the central point was not considered in this analysis as its characteristics was similar to the one obtained from the central point.

During the optimization process, the deflections obtained from each simulation were compared to the deflection obtained from DIC for each iteration. In both SPO and MPO techniques, the values of the parameters were refined to get the least difference with respect to the DIC obtained deflection values. The MPO technique generated a set of non-dominated solutions as there were four objective functions (corresponding to the four points-central point, 0.6 ,0.9, and 1.2 mm from the central point) with equal weighting factors. The solution which gave the least difference between the DIC and iFEM estimated deflection values obtained at the central point was chosen as the optimum solution in case of the MPO technique. Such as choice was linked to the least spatial mismatch of the central point with respect to DIC and FEM, the details of which will be discussed subsequently.

3.2.4 Optimisation results

The true stress-true plastic strain curve estimated by SPO and MPO techniques are compared with the values obtained from the experimental true stress-true plastic strain in Fig. 12. The values of Ludwigson parameters fitted with the actual true-stress true strain data are shown along with these parameters obtained from the SPO and MPO techniques are given in Table 6. The values of 0.2 % proof stress (PS) for both the MPO and SPO techniques were estimated from the engineering stress strain data, back calculated from the true stress-true plastic strain data obtained using the Ludwigson parameters. The ultimate tensile strength (UTS) reported for SPO and MPO techniques were determined from the values of true stress which were equal to the corresponding work hardening rates (slope of the true stress-true strain curve) [59]. The values of actual Youngs modulus and Poisson's ratio were typical values mentioned in ASME standard [60].

Though the value of the 0.2% PS could be obtained with reasonable precision by both SPO and MPO techniques, the values of the elastic constants, UTS and the plastic flow curve derived from MPO technique were in greater agreement with the experimental values as against the values obtained by SPO technique.

9

The maximum in-plane plastic strain distribution in the specimen after punch displacement of 0.6 mm using the optimised elastic and plastic parameters by MPO technique is given in Fig. 13a. The variation of maximum in-plane plastic strain distribution along the SOI for punch displacements ranging from 0.1 to 0.6 mm is given in Fig. 13b. The figure also shows co-ordinate lines drawn at approximate locations were the DIC deflections were obtained. The strain evolution around the pre-deformed distance of 0.6 mm was higher than what was observed at the central point. This finding substantiated the results of strain gradients estimated using KAM maps. The comparison between the load-deflection curves obtained from each of the four locations by FEM using the parameters optimised by MPO technique and DIC is shown in Fig.14. The deviation between the DIC and iFEM results is also indicated in the figure. This deviation was relatively lower at the central and the farthest points when compared to those which were observed at the points which radial distances of 0.6 and 0.9 mm. The cause for higher scatter in the values taken at the radial distances of 0.6 and 0.9 mm is because of the error associated with matching the DIC based positional coordinates to the positional coordinates of the same points in the FEM model.

When the small punch specimen deforms, the radial distances of the three points which were initially placed at distances of 0.6, 0.9 and 1.2 mm from the central point reduces. However, there was no mismatch between the DIC and the FEA coordinates at the central point. Therefore, among the non-dominated solutions of the MPO technique, the solution which had the least difference in the central point was chosen as the optimised solution.

In case of the DIC analysis, the deflections were mapped from fixed locations from the central point throughout the test. However, the deflections in the FEM were taken from the nodes associated with the three pre-deformed positions (0.6, 0.9, 1.2 mm) from the central point. As the deflection values in the FEM were obtained directly from the respective nodes, the change in position of these three points is automatically taken into consideration, which is not the case of the positions from where DIC displacements are obtained. This constituted the mismatch between the positional coordinates of these three points with respect to DIC and FEM analysis.

A retrospective insight on the precision of using MPO technique revealed that the effectiveness of the optimization process depended primarily on the spread of strain values at the points which were chosen for the analysis. Though the SPO technique used deflections from the central point which had no mismatch between the FEM and DIC coordinates, the maximum in-plane strain at this location was only up to a value of 0.105 for punch displacement of 0.6 mm. The MPO technique was more accurate in estimating the tensile properties despite the deviation in positional coordinates as the procedure included deflections from location at 0.6 mm from the central point which had a relatively larger

maximum in-plane strain value of around 0.15 for the same punch displacement. Further, the larger spread of maximum in-plane strain value which ranged from -0.02 (at location of 1.2 mm) to 0.15 (at location of 0.6 mm) made the MPO technique more effective. It should be noted that the deflections obtained through DIC and iFEM from the farthest location (1.2 mm) showed minimal deviation. This is because the maximum in-plane strain values adjacent to this position was relatively constant. Hence the positional variation of this point with respect to DIC and FEA did not enhance the variation of the load-deflection characteristics at this point (Fig. 14).

Though the iFEM based approach could be successfully demonstrated employing DIC deflections up to the onset of Stage III, several improvements in the acquisition system could enhance the applicability this methodology. Designing a more versatile DIC system taking into consideration the uncertainties which arise due to the stereo system and DIC image corrections can help obtain gross deflection contours throughout the course of the test up to the specimen failure. This knowledge would be crucial for comprehensively estimating the damage characteristics of the material.

4. Conclusion

A new system integrating small punch test and digital image correlation was developed for in-situ deflection mapping of the specimen. The systematic errors arising due to the use of the stereo-DIC setup and inclined mirror was estimated using a zero-strain field test. An inverse finite element-based methodology was developed to obtain the elastic and plastic properties of the material using the DIC data. The use of DIC data from multiple point in the small punch specimen gave a closer estimate of the uniaxial tensile properties when compared to the data derived only from the central point on the specimen.

References

[1]   M.P. Manahan, A.S. Argon, O.K. Harling, The development of a miniaturized disk bend test for the determination of postirradiation mechanical properties, J. Nucl. Mater. 104 (1981) 1545–1550. https://doi.org/10.1016/0022-3115(82)90820-0.

[2]   X. Mao, H. Takahashi, Development of a further-miniaturized specimen of 3 mm diameter for tem disk (ø 3 mm) small punch tests, J. Nucl. Mater. 150 (1987) 42–52. https://doi.org/10.1016/0022-3115(87)90092-4.

[3]   T.E. García, C. Rodríguez, F.J. Belzunce, C. Suárez, Estimation of the mechanical properties of metallic materials by means of the small punch test, J. Alloys Compd. 582 (2014) 708–717. https://doi.org/https://doi.org/10.1016/j.jallcom.2013.08.009.

[4]   D. Finarelli, M. Roedig, F. Carsughi, Small punch tests on austenitic and martensitic steels irradiated in a spallation environment with 530 MeV protons, J. Nucl. Mater. 328 (2004) 146–150. https://doi.org/10.1016/j.jnucmat.2004.04.320.

[5]   S. Arunkumar, Overview of Small Punch Test, Met. Mater. Int. (2019). https://doi.org/10.1007/s12540-019-00454-5.

[6]   G.E. Lucas, G.R. Odette, M. Sokolov, P. Spätig, T. Yamamoto, P. Jung, Recent progress in small specimen test technology, J. Nucl. Mater. 307–311 (2002) 1600–1608. https://doi.org/https://doi.org/10.1016/S0022-3115(02)01171-6.

[7]   E. Lucon, Material damage evaluation and residual life assessment of primary power plant components using specimens of non--standard dimensions, Mater. Sci. Technol. 17 (2001) 777–785. https://doi.org/10.1179/026708301101510717.

[8]   M.D. Mathew, J. Ganesh Kumar, V. Ganesan, K. Laha, Small Punch Creep Studies for Optimization of Nitrogen Content in 316LN SS for Enhanced Creep Resistance, Metall. Mater. Trans. A. 45 (2014) 731–737. https://doi.org/10.1007/s11661-013-2027-x.

[9]   D.T. Blagoeva, R.C. Hurst, Application of the CEN (European Committee for Standardization) small punch creep testing code of practice to a representative repair welded P91 pipe, Mater. Sci. Eng. A. 510–511 (2009) 219–223. https://doi.org/https://doi.org/10.1016/j.msea.2008.05.058.

[10]   E. Fleury, J.S. Ha, Small punch tests to estimate the mechanical properties of steels for steam power plant: I. Mechanical strength, Int. J. Press. Vessel. Pip. 75 (1998) 699–706. https://doi.org/https://doi.org/10.1016/S0308-0161(98)00074-X.

[11]   M. Bruchhausen, S. Holmström, I. Simonovski, T. Austin, J.-M. Lapetite, S. Ripplinger, F. de Haan, Recent developments in small punch testing: Tensile properties and DBTT, Theor. Appl. Fract. Mech. 86 (2016) 2–10. https://doi.org/https://doi.org/10.1016/j.tafmec.2016.09.012.

[12]   F. Dobeš, P. Dymáček, M. Besterci, Estimation of the mechanical properties of aluminium and an aluminium composite after equal channel angular pressing by means of the small punch test, Mater. Sci. Eng. A. 626 (2015) 313–321. https://doi.org/https://doi.org/10.1016/j.msea.2014.12.054.

[13]   Y. Xu, Z. Zhao, A Modified Miniature Disk Test for Determining Material Mechanical Properties, J. Test. Eval. 23 (1995) 300–306. https://doi.org/10.1520/JTE10429J.

[14]   Y. Ruan, P. Spätig, M. Victoria, Assessment of mechanical properties of the martensitic steel EUROFER97 by means of punch tests, J. Nucl. Mater. 307–311 (2002) 236–239. https://doi.org/https://doi.org/10.1016/S0022-3115(02)01194-7.

[15]   M. Eskner, R. Sandström, Mechanical Property Evaluation Using the Small Punch Test, J. Test. Eval. 32 (2004) 282–289. https://doi.org/10.1520/JTE11504.

[16]   E. Altstadt, M. Houska, I. Simonovski, M. Bruchhausen, S. Holmström, R. Lacalle, On the estimation of ultimate tensile stress from small punch testing, Int. J. Mech. Sci. 136 (2018) 85–93. https://doi.org/https://doi.org/10.1016/j.ijmecsci.2017.12.016.

[17]   A. Husain, D.K. Sehgal, R.K. Pandey, An inverse finite element procedure for the determination of constitutive tensile behavior of materials using miniature specimen, Comput. Mater. Sci. 31 (2004) 84–92. https://doi.org/https://doi.org/10.1016/j.commatsci.2004.01.039.

[18]   I. Peñuelas, I.I. Cuesta, C. Betegón, C. Rodriguez, F.J. Belzunce, Inverse determination of the elastoplastic and damage parameters on small punch tests, Fatigue Fract. Eng. Mater. Struct. 32 (2009) 872–885. https://doi.org/10.1111/j.1460-2695.2009.01387.x.

[19]   M. Abendroth, M. Kuna, Identification of ductile damage and fracture parameters from the small punch test using neural networks, Eng. Fract. Mech. 73 (2006) 710–725. https://doi.org/https://doi.org/10.1016/j.engfracmech.2005.10.007.

[20]   J. Zhong, T. Xu, K. Guan, J. Szpunar, A procedure for predicting strength properties using small punch test and finite element simulation, Int. J. Mech. Sci. 152 (2019) 228–235. https://doi.org/10.1016/j.ijmecsci.2019.01.006.

[21]   S. Yang, Y. Cao, X. Ling, Y. Qian, Assessment of mechanical properties of Incoloy800H by means of small punch test and inverse analysis, J. Alloys Compd. 695 (2017) 2499–2505. https://doi.org/https://doi.org/10.1016/j.jallcom.2016.11.151.

[22]   J.-S. Cheon, C.-H. Joo, Small punch test for determining a flow stress by using a hybrid inverse procedure, Comput. Mater. Sci. 43 (2008) 744–751. https://doi.org/https://doi.org/10.1016/j.commatsci.2008.01.052.

[23]   A. Lotfolahpour, N. Soltani, M. Ganjiani, D. Baharlouei, Parameters identification and validation of plastic-damage model of 304 stainless steel by small punch test at ambient temperature, Eng. Fract. Mech. 200 (2018) 64–74. https://doi.org/https://doi.org/10.1016/j.engfracmech.2018.07.007.

[24]   J.C. Chica, P.M. Bravo Díez, M. Preciado Calzada, Improved correlation for elastic modulus prediction of metallic materials in the Small Punch Test, Int. J. Mech. Sci. 134 (2017) 112–122. https://doi.org/https://doi.org/10.1016/j.ijmecsci.2017.10.006.

[25]   E. Priel, B. Mittelman, S. Haroush, A. Turgeman, R. Shneck, Y. Gelbstein, Estimation of yield and ultimate stress using the small punch test method applied to non-standard specimens: A computational study validated by experiments, Int. J. Mech. Sci. 135 (2018) 484–498. https://doi.org/https://doi.org/10.1016/j.ijmecsci.2017.11.040.

[26]   K. Li, J. Peng, C. Zhou, Construction of whole stress-strain curve by small punch test and inverse finite element, Results Phys. 11 (2018) 440–448. https://doi.org/https://doi.org/10.1016/j.rinp.2018.09.024.

[27]   K. Kumar, A. Pooleery, K. Madhusoodanan, R.N. Singh, J.K. Chakravartty, R.S. Shriwastaw, B.K. Dutta, R.K. Sinha, Evaluation of ultimate tensile strength using Miniature Disk Bend Test, J. Nucl. Mater. 461 (2015) 100–111. https://doi.org/https://doi.org/10.1016/j.jnucmat.2015.02.029.

[28]   B. Gülçimen, P. Hähner, Determination of creep properties of a P91 weldment by small punch testing and a new evaluation approach, Mater. Sci. Eng. A. 588 (2013) 125–131.

https://doi.org/https://doi.org/10.1016/j.msea.2013.09.029.

[29]   S. Yang, X. Ling, Y. Zheng, Creep behaviors evaluation of Incoloy800H by small punch creep test, Mater. Sci. Eng. A. 685 (2017) 1–6. https://doi.org/10.1016/j.msea.2016.12.092.

[30]   F. Cortellino, J.P. Rouse, B. Cacciapuoti, W. Sun, T.H. Hyde, Experimental and Numerical Analysis of Initial Plasticity in P91 Steel Small Punch Creep Samples, Exp. Mech. 57 (2017) 1193–1212. https://doi.org/10.1007/s11340-017-0296-9.

[31]   Y. Xu, K. Guan, Evaluation of fracture toughness by notched small punch tests with Weibull stress method, Mater. Des. 51 (2013) 605–611. https://doi.org/https://doi.org/10.1016/j.matdes.2013.04.071.

[32]   J. Foulds, P. Woytowitz, T. Parnell, C. Jewett, Fracture Toughness by Small Punch Testing, J. Test. Eval. 23 (1995) 3–10. https://doi.org/10.1520/JTE10392J.

[33]   J.-Y. Jeon, Y.-J. Kim, S.-Y. Lee, J.-W. Kim, Extracting ductile fracture toughness from small punch test data using numerical modeling, Int. J. Press. Vessel. Pip. 139–140 (2016) 204–219. https://doi.org/https://doi.org/10.1016/j.ijpvp.2016.02.011.

[34]   J.K. J-M Baik O Buck, Development of Small Punch Tests for Ductile-Brittle Transition Temperature Measurement of Temper Embrittled Ni-Cr Steels, ASTM International, West Conshohocken, PA, n.d. https://doi.org/10.1520/STP32997S.

[35]   X. Gai, Y.S. Sato, H. Kokawa, K. Ichikawa, Ductile-brittle transition of steel electron beam weld metal in small punch test, Sci. Technol. Weld. Join. 7 (2002) 204–211. https://doi.org/10.1179/136217102225004275.

[36]   K. Guan, D. Wang, J. Dobrovská, K. Matocha, Evaluation of the ductile-brittle transition temperature of anisotropic materials by small punch test with un-notched and U-notched specimens, Theor. Appl. Fract. Mech. 102 (2019) 98–102. https://doi.org/https://doi.org/10.1016/j.tafmec.2019.04.003.

[37]   R.J. Lancaster, S.P. Jeffs, H.W. Illsley, C. Argyrakis, R.C. Hurst, G.J. Baxter, Development of a novel methodology to study fatigue properties using the small punch test, Mater. Sci. Eng. A. 748 (2019) 21–29. https://doi.org/https://doi.org/10.1016/j.msea.2019.01.074.

[38]   CEN workshop agreement, CWA, Small punch test method for metallic materials, (2007) Brussels, Belgium.

[39]   P.F. Luo, Y.J. Chao, M.A. Sutton, W.H. Peters, Accurate measurement of three-dimensional deformations in deformable and rigid bodies using computer vision, Exp. Mech. 33 (1993) 123–132. https://doi.org/10.1007/BF02322488.

[40]   D. Garcia, J.J. Orteu, L. Penazzi, A combined temporal tracking and stereo-correlation technique for accurate measurement of 3D displacements: application to sheet metal forming, J. Mater. Process. Technol. 125–126 (2002) 736–742. https://doi.org/https://doi.org/10.1016/S0924-0136(02)00380-1.

[41]   B. Pan, W. Shi, G. Lubineau, Effect of camera temperature variations on stereo-digital image correlation measurements, Appl. Opt. 54 (2015) 10089–10095. https://doi.org/10.1364/AO.54.010089.

[42]   S. Amini, R.S. Kumar, A high-fidelity strain-mapping framework using digital image correlation, Mater. Sci. Eng. A. 594 (2014) 394–403. https://doi.org/https://doi.org/10.1016/j.msea.2013.11.020.

[43] G. Di Leo, C. Liguori, A. Paolillo, Propagation of uncertainty through stereo triangulation, in: 2010 IEEE Instrum. Meas. Technol. Conf. Proc., 2010: pp. 12–17. https://doi.org/10.1109/IMTC.2010.5488057.

[44] R. Balcaen, P.L. Reu, P. Lava, D. Debruyne, Stereo-DIC Uncertainty Quantification based on Simulated Images, Exp. Mech. 57 (2017) 939–951. https://doi.org/10.1007/s11340-017-0288-9.

[45] Y. Su, Q. Zhang, X. Xu, Z. Gao, Quality assessment of speckle patterns for DIC by consideration of both systematic errors and random errors, Opt. Lasers Eng. 86 (2016) 132–142. https://doi.org/https://doi.org/10.1016/j.optlaseng.2016.05.019.

[46] J.C.M. Antón, J. Alonso, J.A.G. Pedrero, Topographic optical profilometry of steep slope micro-optical transparent surfaces, Opt. Express. 23 (2015) 9494. https://doi.org/10.1364/oe.23.009494.

[47] I.I. Cuesta, J.M. Alegre, R. Lacalle, Determination of the Gurson-Tvergaard damage model parameters for simulating small punch tests, Fatigue Fract. Eng. Mater. Struct. 33 (2010) 703–713. https://doi.org/10.1111/j.1460-2695.2010.01481.x.

[48] D. Jorge-Badiola, A. Iza-Mendia, I. Gutiérrez, Evaluation of intragranular misorientation parameters measured by EBSD in a hot worked austenitic stainless steel, 2007. https://doi.org/10.1111/j.1365-2818.2007.01850.x.

[49] V.D. Vijayanand, J. Vanaja, C.R. Das, K. Mariappan, A. Thakur, S. Hussain, G.V.P. Reddy, G. Sasikala, S.K. Albert, An investigation of microstructural evolution in electron beam welded RAFM steel and 316LN SS dissimilar joint under creep loading conditions, Mater. Sci. Eng. A. 742 (2019) 432–441. https://doi.org/https://doi.org/10.1016/j.msea.2018.11.046.

[50] M. KAMAYA, K. KUBUSHIRO, Y. SAKAKIBARA, S. SUZUKI, H. MORITA, R. YODA, D. KOBAYASHI, K. YAMAGIWA, T. NISHIOKA, Y. YAMAZAKI, Y. KAMADA, T. HANADA, T. OHTANI, Round robin crystal orientation measurement using EBSD for damage assessment, Mech. Eng. J. 3 (2016) 16-00077-16–00077. https://doi.org/10.1299/mej.16-00077.

[51] C.S. Catherine, J. Messier, C. Poussard, S. Rosinski, J. Foulds, Small punch test: EPRI-CEA finite element simulation benchmark and inverse method for the estimation of elastic plastic behavior, ASTM Spec. Tech. Publ. (2002) 350–370.

[52] D.C. Ludwigson, Modified stress-strain relation for FCC metals and alloys, Metall. Trans. 2 (1971) 2825–2828. https://doi.org/10.1007/BF02813258.

[53] E. Isaac Samuel, B.K. Choudhary, Universal scaling of work hardening parameters in type 316L(N) stainless steel, Mater. Sci. Eng. A. 527 (2010) 7457–7460. https://doi.org/https://doi.org/10.1016/j.msea.2010.08.021.

[54] K.G. Samuel, P. Rodriguez, On power-law type relationships and the Ludwigson explanation for the stress-strain behaviour of AISI 316 stainless steel, J. Mater. Sci. 40 (2005) 5727–5731. https://doi.org/10.1007/s10853-005-1078-9.

[55] S. Wang, K. Yang, Y. Shan, L. Li, Plastic deformation and fracture behaviors of nitrogen-alloyed austenitic stainless steels, Mater. Sci. Eng. A. 490 (2008) 95–104. https://doi.org/https://doi.org/10.1016/j.msea.2008.01.015.

[56] V.D. Vijayanand, K. Laha, P. Parameswaran, M. Nandagopal, S. Panneer Selvi, M.D. Mathew, Influence of thermo-mechanical treatment on the tensile properties of a modified 14Cr-15Ni stainless steel, J. Nucl. Mater. 453 (2014). https://doi.org/10.1016/j.jnucmat.2014.06.067.

[57] T. Li, J. Zheng, Z. Chen, Description of full-range strain hardening behavior of steels, Springerplus. 5 (2016) 1316. https://doi.org/10.1186/s40064-016-2998-3.

[58] S.N. Sivanandam, S.N. Deepa, Genetic Algorithms BT - Introduction to Genetic Algorithms, in: S.N. Sivanandam, S.N. Deepa (Eds.), Springer Berlin Heidelberg, Berlin, Heidelberg, 2008: pp. 15–37. https://doi.org/10.1007/978-3-540-73190-0_2.

[59] G.E. Dieter, D. Bacon, Mechanical Metallurgy, McGraw-Hill, 1988. https://books.google.co.uk/books?id=hlabmB3e8XwC.

[60] ASME Boiler and Pressure Vessel Code, Section II, Part D, 2019. The American Society of Mechanical Engineers New York, New York, USA., (n.d.).

List of Tables

Table 1. Chemical Composition (in wt.%)

	C	Cr	Ni	Mo	Mn	Si	N	S	Si	P	Al	Fe
316L	0.019	16.84	11.29	2.10	1.46	0.52	0.072	0.001	0.52	0.038	0.001	Bal.

Table 2 Principal dimensions of the small punch test rig

Part	Symbol	Dimension (mm)
Ceramic Ball Radius	r	1.25
Chamfer Length & Angle	c	0.2, 45°
Receiving Hole Diameter	D	4
Specimen Diameter	D_s	8
Specimen Thickness	h_0	0.5

Table 3 Details of the stereo DIC set up and calibration

Camera Resolution	2464 x 2056 pixel
Lens Magnification	0.3 x
Lens Working distance	236 mm
Numerical Aperture	0.03
Stereo Angle	5.8°
Base line distance	22 mm
Image scale factor	234.116 pixels/mm
Standard deviation of fit	1.37 pixels
Calibrated Field of view	10×8.7 mm^2

Table 4 Upper and Lower bounds of parameter values

	K_1	n_1	K_2	n_2	E (GPa)	v
Lower Bound	1200	0.25	5.1	-8	185	0.26
Upper Bound	1700	1	6.2	-2	205	0.32

Table 5 Genetic Algorithm options set during the optimisation process

Population Size	50
Generations	20
Initial Population	Random
Selection function	Stochastic Uniform
Elite Count	2
Crossover Fraction	0.8
Crossover Function	Scattered
Fitness Scaling	Rank based
Mutation function	Gaussian

Table 6 Comparison of the parameters obtained from experimental, multi point (MPO) and single point optimisation (SPO) iFEM techniques

	K_1	n_1	K_2	n_2	E (GPa)	v	0.2% PS (MPa)	UTS (MPa)
Experimental	1558	0.74	5.41	-4.63	195	0.31	229	595
MPO	1483	0.69	5.36	-3.89	196.6 (+0.82%)	0.3 (-3.26%)	233 (1.75%)	585 (-1.68%)
SPO	1679	0.71	5.33	-4.61	199.2 (+2.15%)	0.26 (-16.13%)	223 (-2.62%)	650 (9.24%)
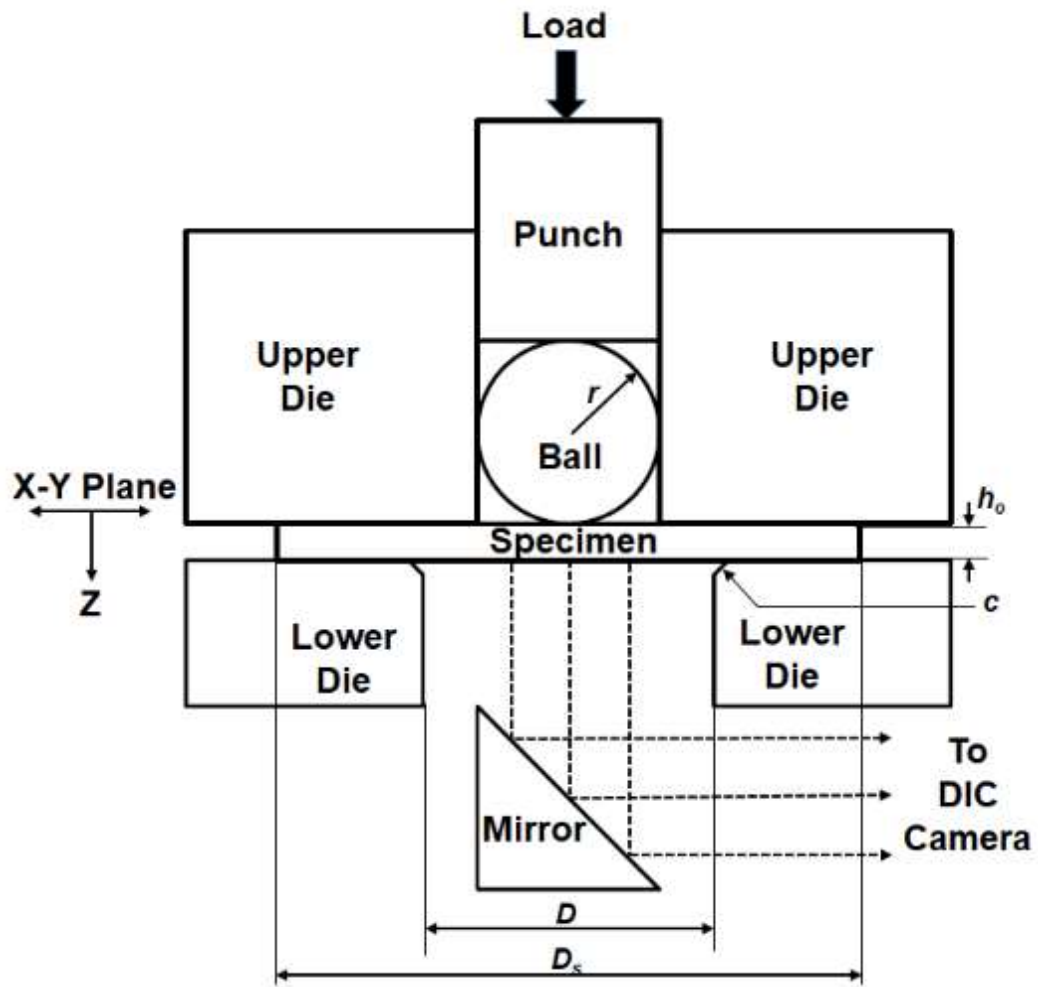
Fig. 1. Schematic of the small punch test rig, r=radius of the ceramic ball, c=chamfer, D= diameter of the receiving hole, D_s=specimen diameter, h_o=specimen thickness.
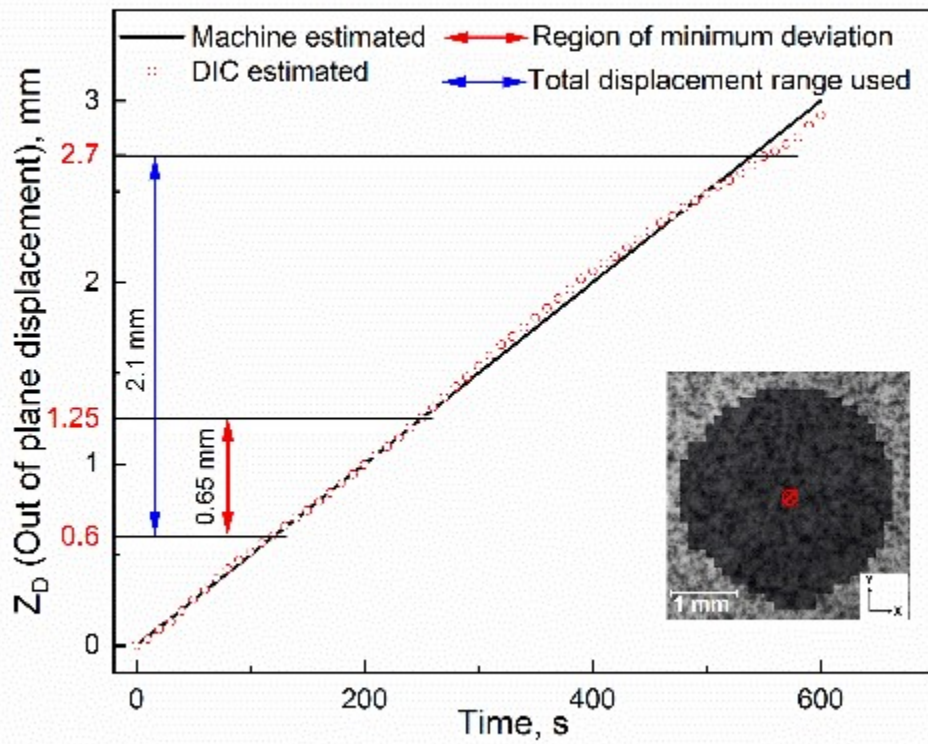
Fig.2. Comparison between the machine and DIC estimated displacements taken from the central point of the region of interest. The region of minimum deviation (variation =±0.01 mm) and the total displacement range (variation =±0.07 mm) used in this study is also indicated.
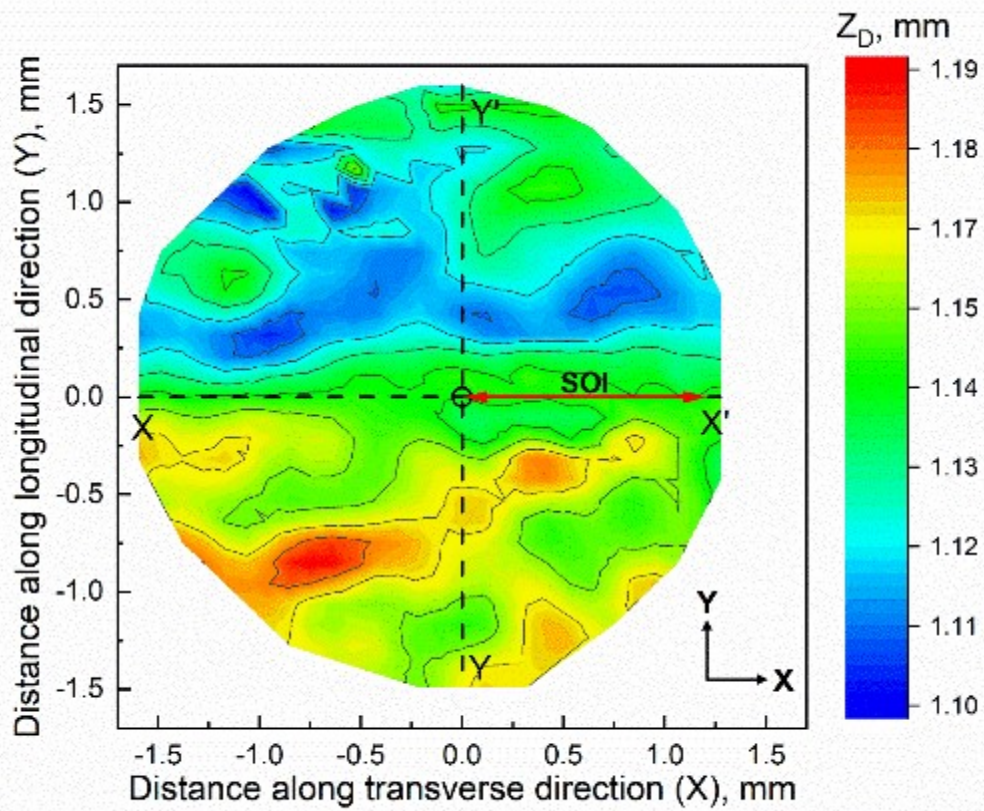
Fig. 3. Displacement contours obtained after a machine estimated displacement of 1.15 mm. The segment of interest (SOI) which was used in the subsequent analysis is also depicted.
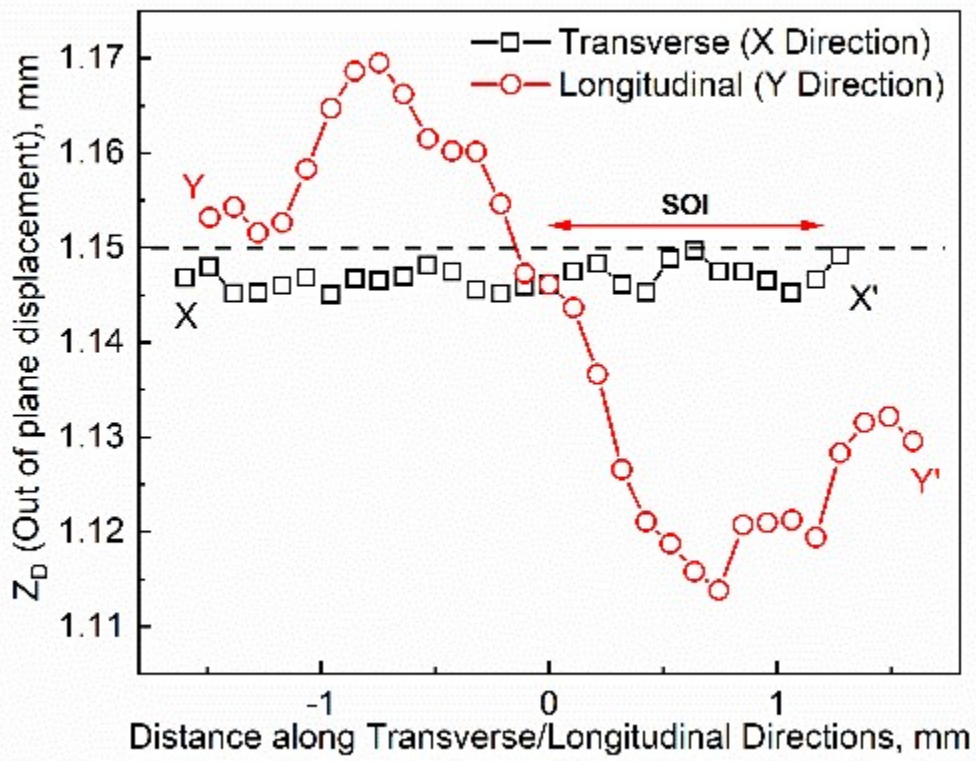
Fig. 4. Scatter in DIC estimated displacements along the transverse and longitudinal directions with respect to machine estimated displacement of 1.15 mm. The segment of interest (SOI) which was used in the subsequent analysis is also depicted.
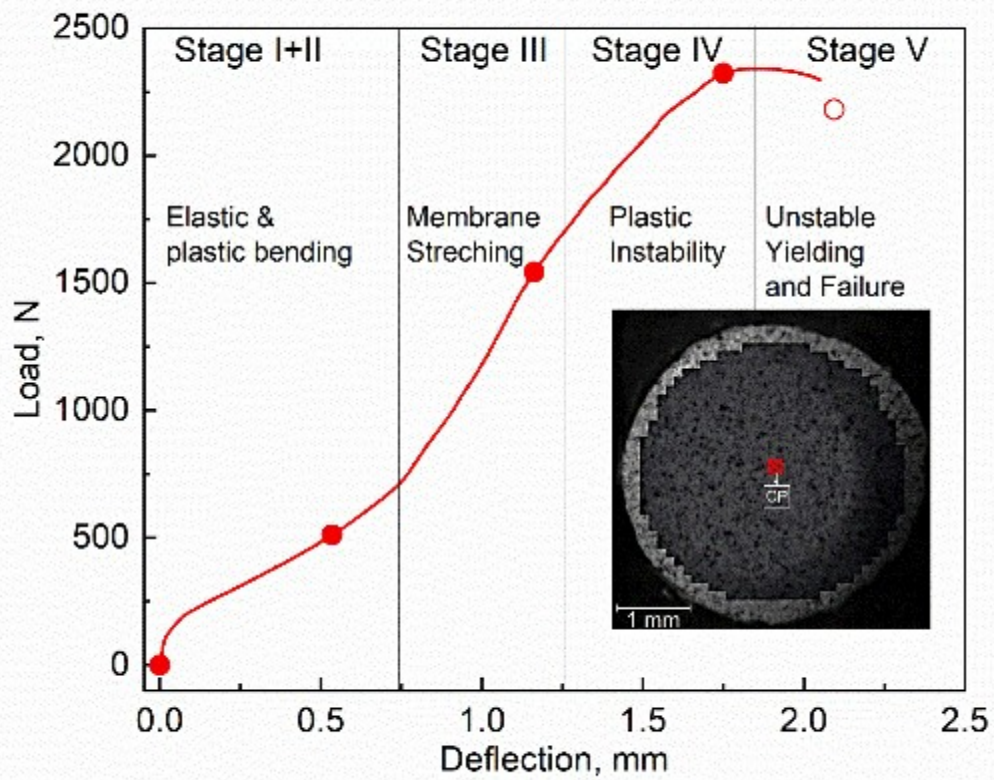
Fig. 5. Load-deflection (LD) curve taken from the central point (CP) of the ROI showing stages corresponding to various deformation modes. The red data points on the LD graph correspond to instances at which DIC-analysed images are depicted subsequently.
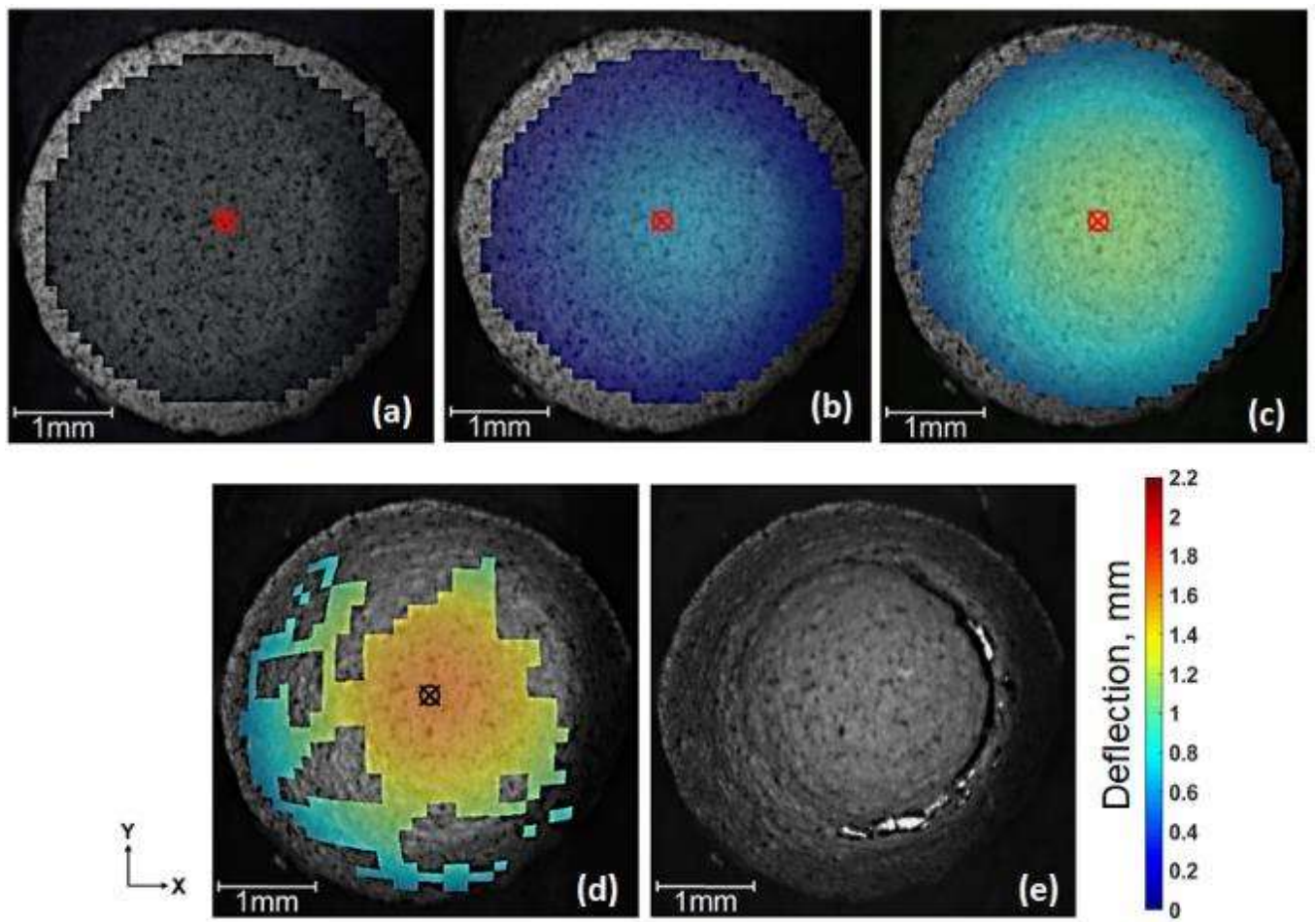
Fig.6. DIC estimated contours taken at central point (CP) deflections of a) 0 mm, b) 0.54 mm, c) 1.16 mm, d) 1.75 mm and e) image after failure.
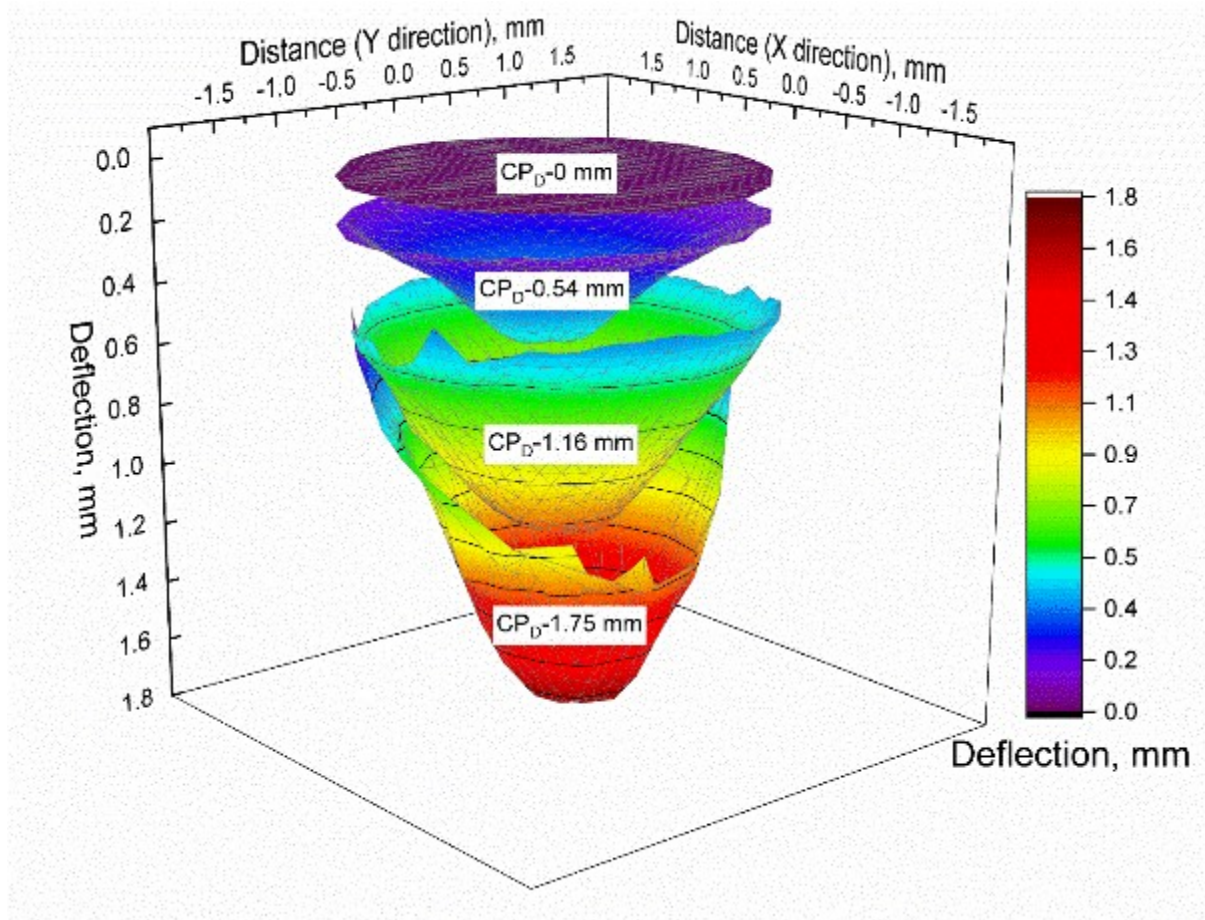
Fig. 7. DIC estimated 3D contour maps taken at central point deflections (CP$_D$) of 0 mm, 0.54 mm, 1.16 mm and 1.75 mm
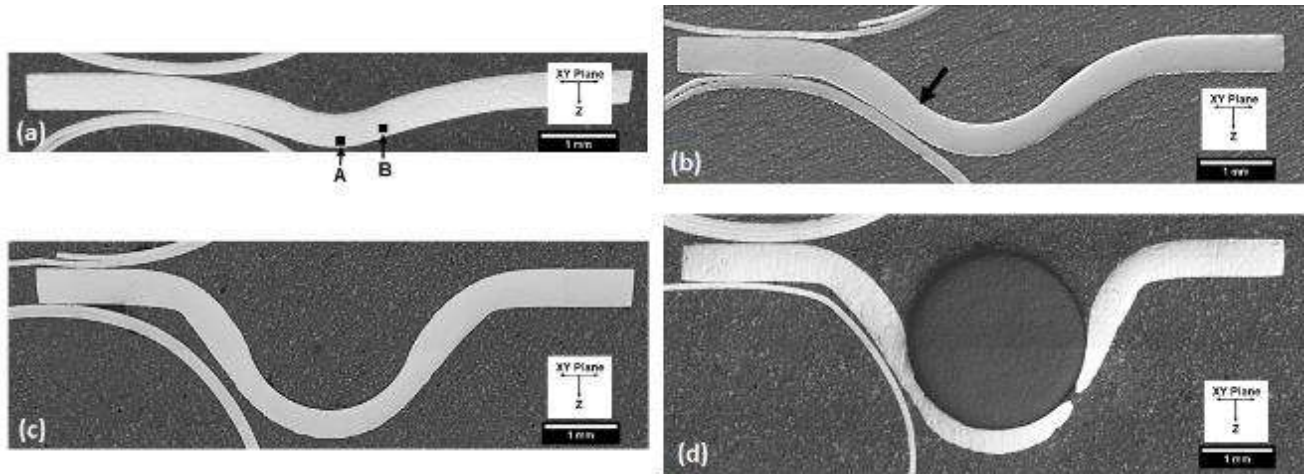
Fig. 8. Macrographs of the small specimens interrupted at approximate centre point deflections of a) 0.54 mm, b) 1.16 mm, c) 1.75 mm and d) failed specimen. The regions were EBSD analysis was done on the specimen deflected of 0.54 mm is indicated. The onset of localised thinning is shown in the specimen deflected to 1.16 mm.
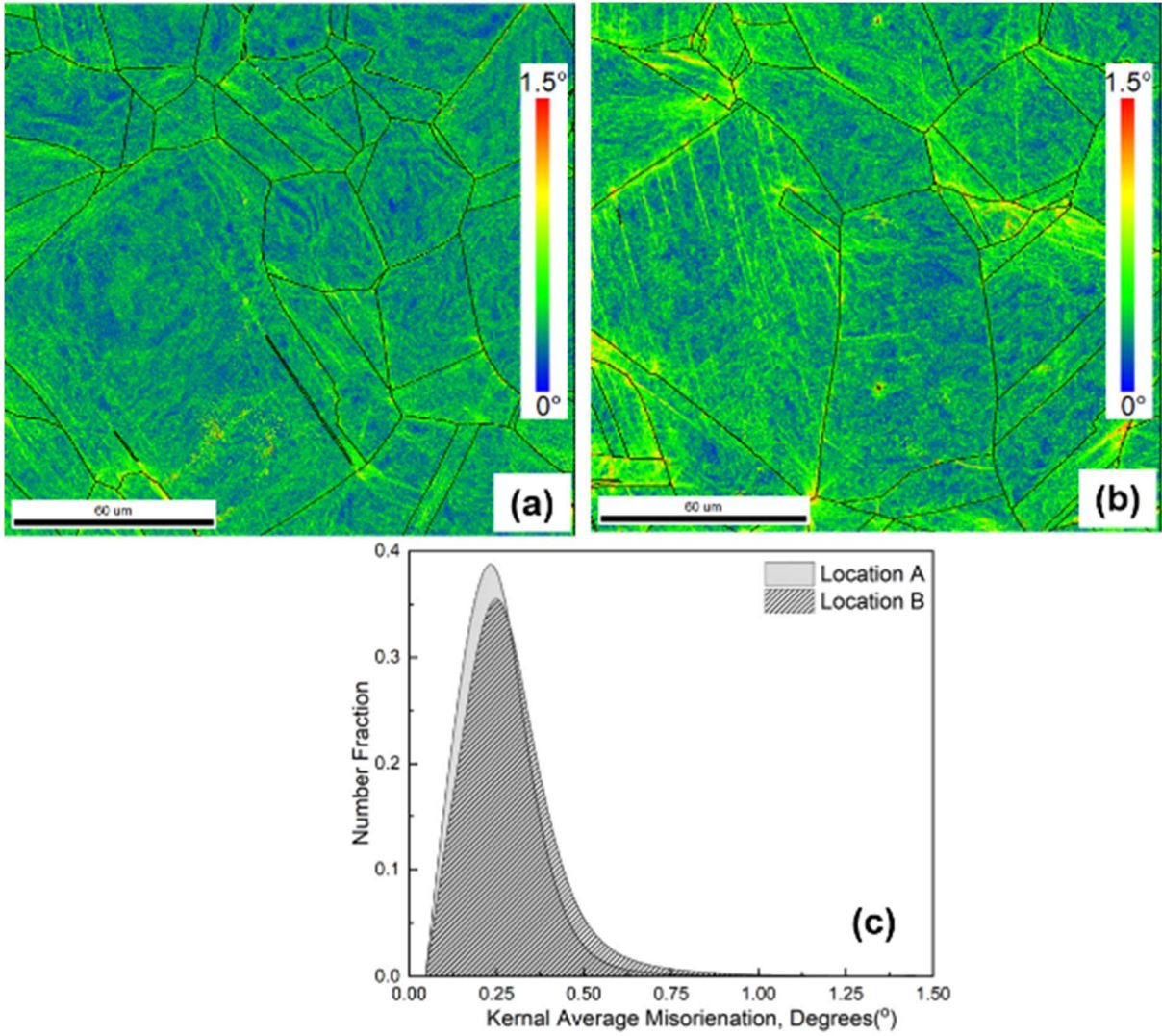
Fig. 9. Kernel Average Misorientation (KAM) maps taken at a) location A b) location B on the specimen deflected up to approximately 0.54 mm and c) KAM distribution for various misorientation angles in these two locations.
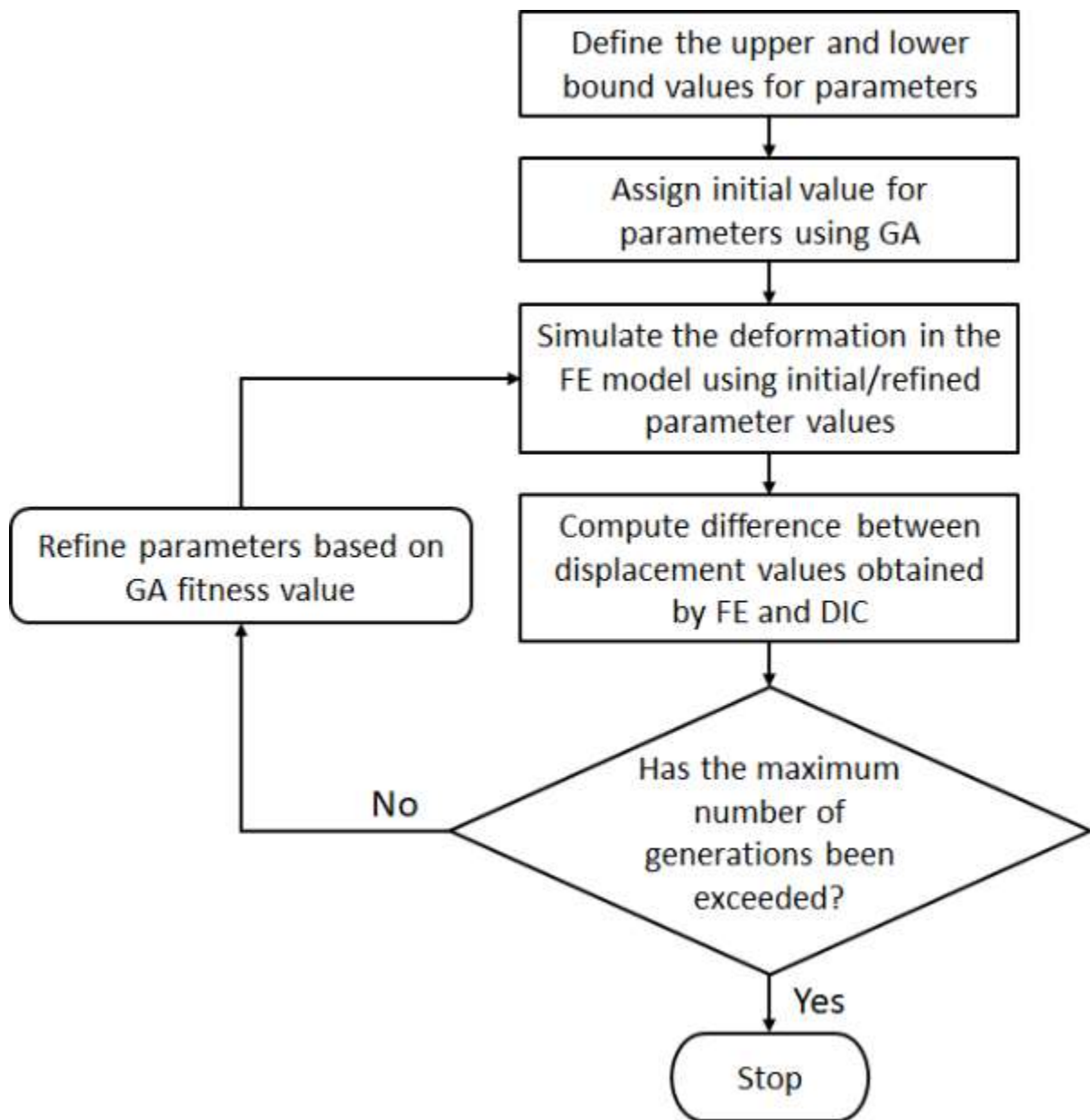
Fig. 10. Scheme for inverse finite element method (iFEM) depicting genetic algorithm (GA) based methodology incorporating displacements obtained from finite element (FE) and digital image correlation (DIC)
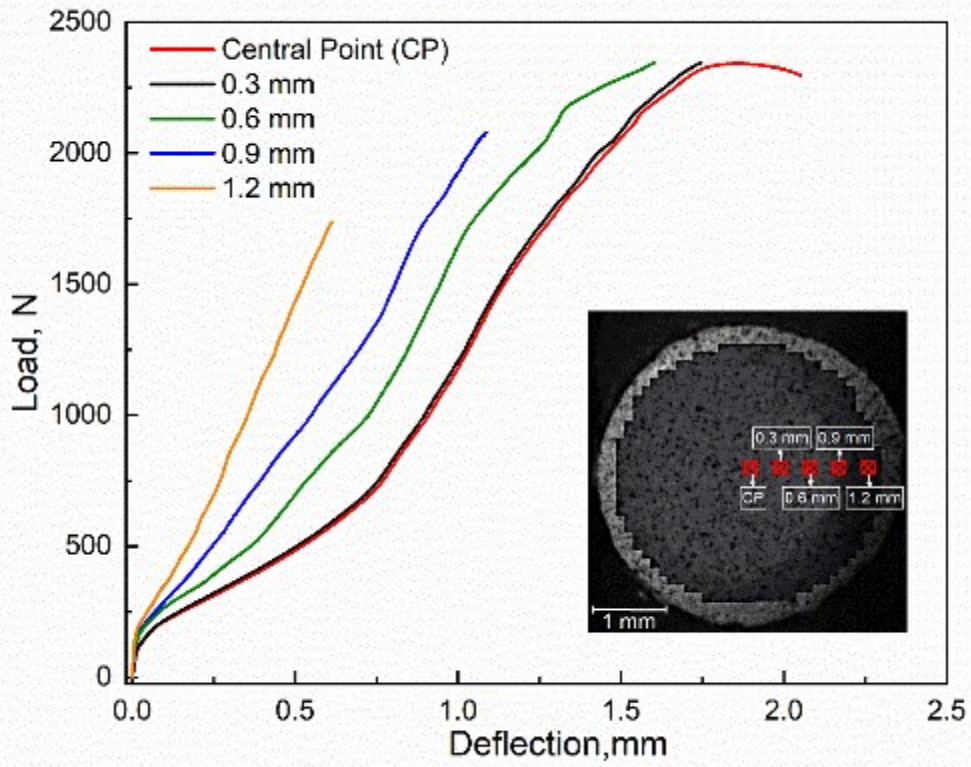
Fig. 11 Load-deflection curves taken from the central point (CP) and at locations at a distance of 0.3 mm, 0.6 mm, 0.9 mm and 1.2 mm from CP.
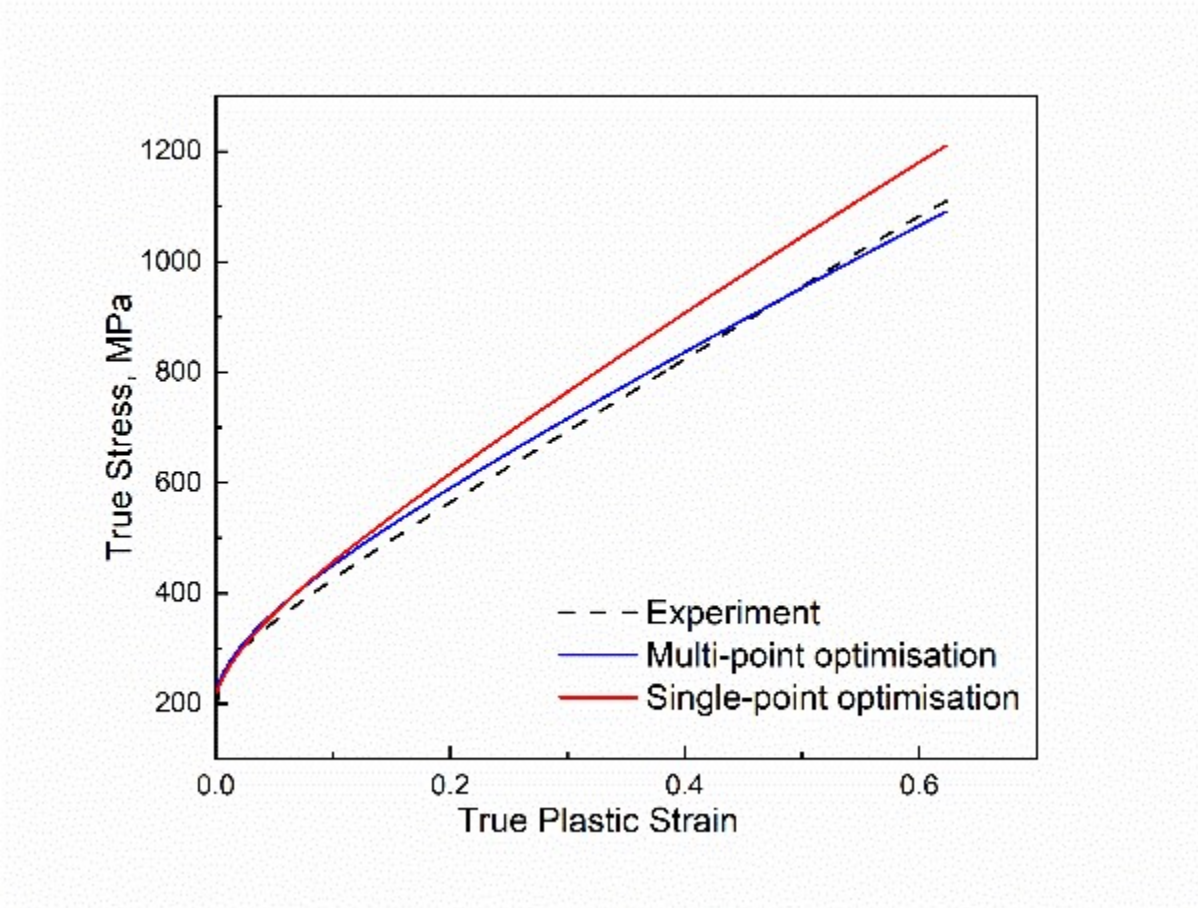
Fig. 12 Comparison of the experimental true stress-true plastic strain curves with the true stress-true plastic strain curves estimated by single point optimisation (SPO) and multiple point optimisation (MPO) techniques.
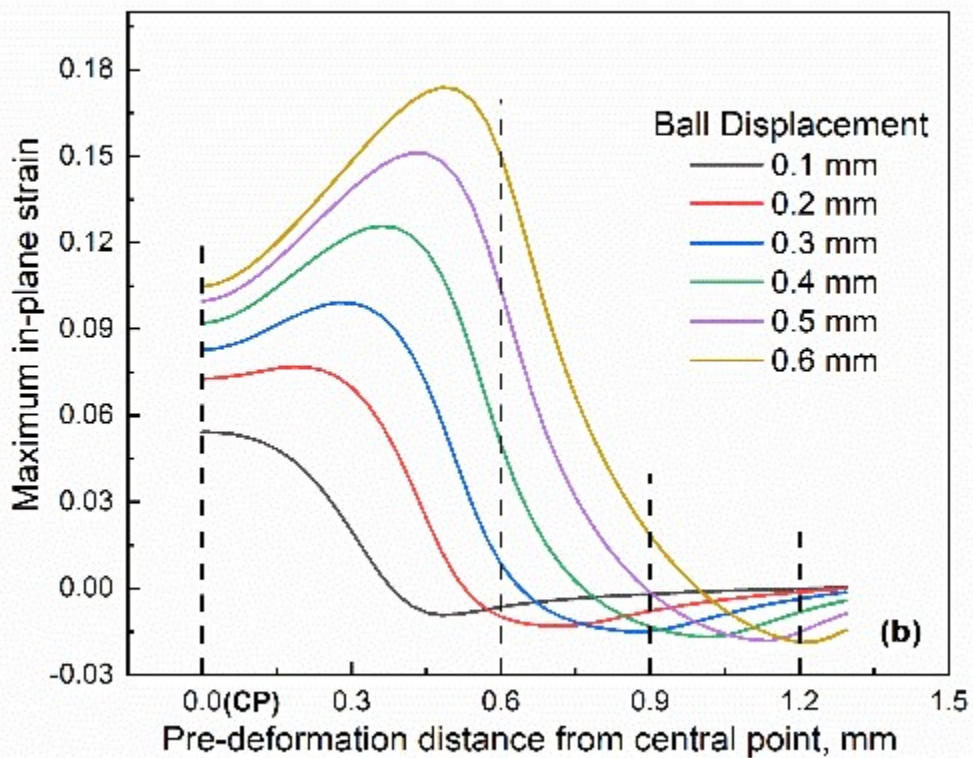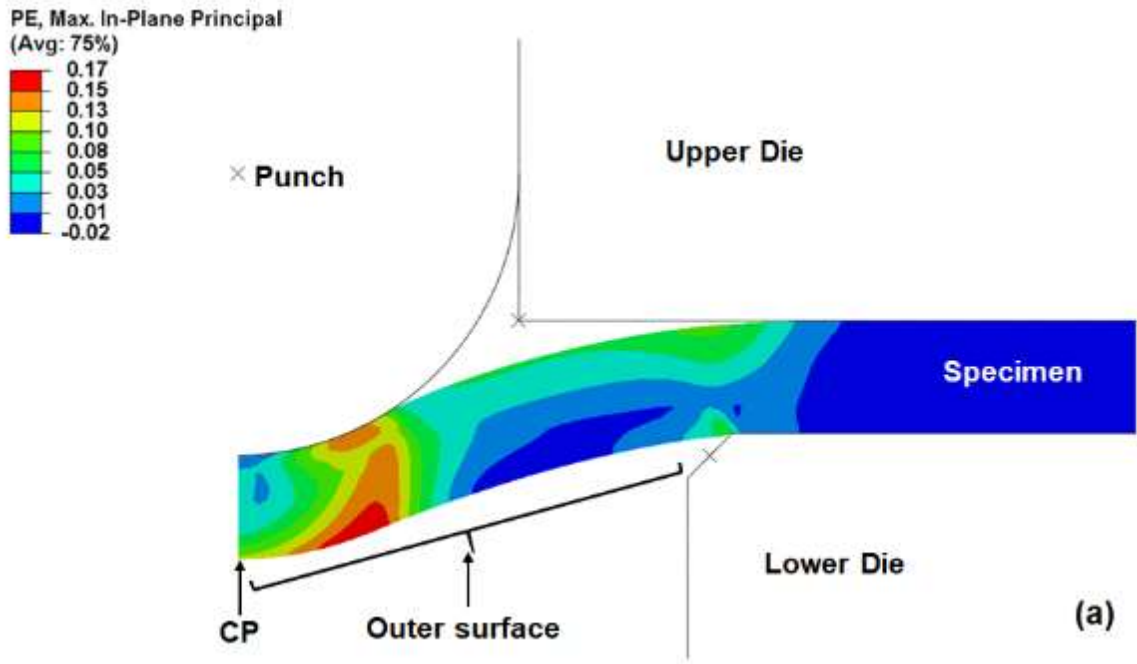
Fig. 13 a) Maximum in-plane strain contour specimen after punch displacement of 0.60 mm and b) maximum in-plane strain distribution on the outer surface of the specimen for punch displacements ranging from of 0.1 to 0.6 mm. The location of the central point (CP) is shown in both the figures.
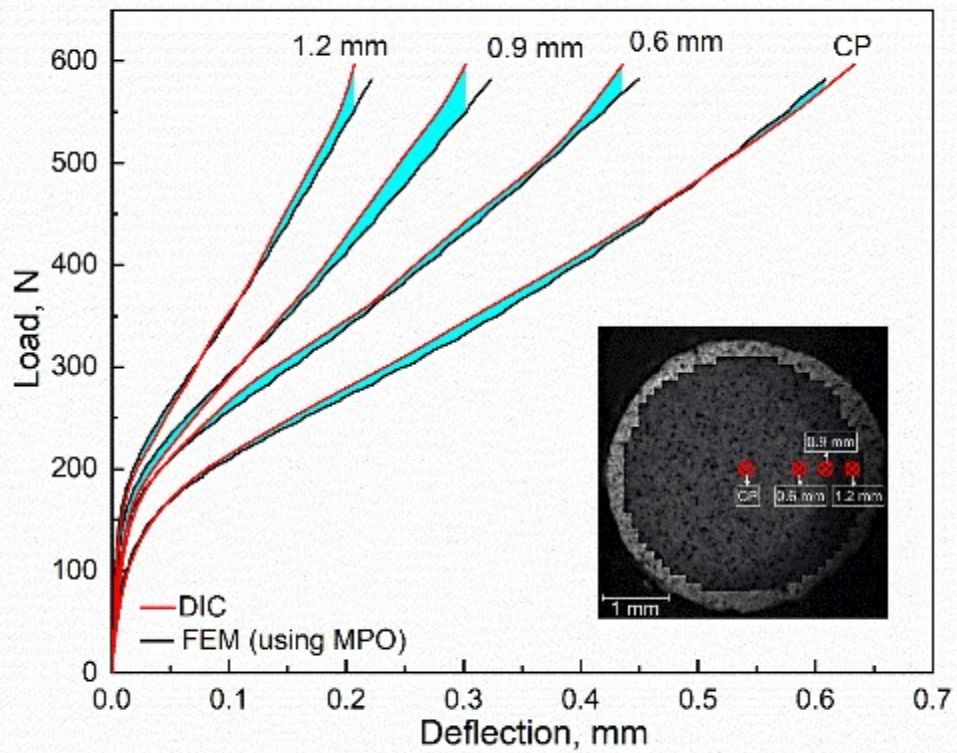
Fig. 14 Comparison of the load-deflection curves obtained by FEM using parameters optimised by multiple point optimisation (MPO) technique and DIC. The mismatch between the DIC and FEM data at each of the points is highlighted.